# Chapter-5

# Electrochemical performance of A-site substituted $SmSrNiO_{4-\delta}$

**Publication:** ***Manisha Chauhan, Ajay S. Bangwal, and Prabhakar singh, Int. J. Hydrogen energy,"Electrochemical performance of A-site substituted*** $SmSrNiO_{4-\delta}$ ***" : Accepted***

# CHAPTER 5: Electrochemical performance of A-site substituted $SmSrNiO_{4-\delta}$ for energy storage applications

## 5.1 Introduction

In recent years, with the rapid growth of the market for portable electronic devices and electrical vehicle, high density energy devices have gained larger popularity[215]. This is the reason battery and Electrochemical energy storage capacitors are considered promising alternatives for the sustainable energy system for the near future and widely investigated in scientific community[204][205]. However, none of these devices can fulfill the demand of power and energy density by alone itself. This brings the concept of supercapacitor in limelight. Supercapacitors (SCs) are gaining much attentions in scientific world because of its high-power density(higher than conventional battery), fast charge-discharge rate, improved safety, high energy density (higher than traditional capacitors) and environmental friendliness[206],[207]. SCs can be divided into two categories based upon the active materials used and charge storage mechanism: First one is Electrochemical double layer capacitor (EDLC), which is most common device, stored charge without any electrochemical reactions. Second group of SCs is pseudo-capacitor, which stores charge through faradic redox reaction or ion intercalation. A hybrid capacitor is latest kind of SCs, which combine a capacitive electrode and faradic electrode either in aquas based electrolytes or organic based electrolyte. Thus, hybrid capacitors have benefit of both capacitor and battery properties.

Ruddlesden-popper oxides (RP) are attracting the research attentions as a new type of layered perovskite derivatives. The general formula of RP structure is $A_{n+1}B_nO_{3n+1}$, which consist of a perovskite-like layers ($ABO_3$) with an alternating rock-salt layers (AO) along the

crystallographic c-axis direction. RP perovskites have been shown to have a variety of functional properties that are either distinct from or completely missing in simple perovskite, depending on the nature of the constituent elements. These properties are superconductivity[220], piezoelectricity[221], ferromagnetism[222], magnetoresistance[222] and photocatalytic activity[223]. Furthermore, RP perovskite has also been widely reported with fascinating catalytic properties for electrocatalysis offering a variety of chemical transformations, such as Oxygen evolution reaction (OER),Oxygen reduction reaction (ORR), Hydrogen evolutions, $CO_2/H_2O$ reduction for high temperature electrochemical devices such as Solid oxide electrolyzer cells (SOECs), Solid oxide fuel cells (SOFCs), and also for the low temperature electrochemical devices such as metal-air batteries and electrolysis cells. In recent years, interestingly research on RP has been shifted to utilize their applications for energy storage devices, like $La_2NiO_{4+\delta}$ as a pseudocapacitive electrode[224], Ag-nanoparticle coated $La_2NiO_{4+\delta}$ as a hybrid supercapacitor[225], $LaSr_2Mn_2O_7$ as an active electrode for electrochemical capacitors[226] and $Sr_xCa_{3-x}GaMn_2O_8$ as a pseudo-capacitor[227]. However, the application of RP oxides as an energy storage device is less explored and similarly compositional variation of RP oxide is also least investigated.

The RP perovskite with general formula $Ln_2NiO_{4+\delta}$ (Ln = La, Pr, Sm and Nd) is highly sensitive to oxygen stoichiometry, which is strongly influenced by dopant types. The hole (Sr) substitution in $Ln_2NiO_{4+\delta}$($Ln_{2-x}Sr_xNiO_{4+\delta}$) leading to the phase change, which affect the electrocatalytic properties as well[228]. The same phenomena was also observed in $Sm_{2-x}Sr_xNiO_{4-\delta}$ [229]. This implies that the electrochemical behavior can be significantly influenced by the A-site doping. With a proper substitution amount, electrochemical performance of the traditional perovskites can be enhanced[230]–[233]. Thus, in this chapter, the effect of co-

doping (La and Ca) on the electrochemical behavior of $SmSrNiO_{4-\delta}$ was studied. For this purpose, we reported a novel series of electrode $Sm_{1-x}La_xSr_{1-x}Ca_xNiO_{4-\delta}$ (x = 0.00, 0.05, 0.10, 0.15 and 0.20) synthesized through solid state route. The electrodes were characterized through Thermogravimetry analysis (TGA), X-ray diffraction (XRD), Fourier Transform Infrared spectroscopy (FTIR), and scanning electron microscopy (SEM). The electrochemical performance of the electrodes was investigated through Cyclic voltammetry (CV) and the reason of their better electrochemical behavior was analyzed through X-ray diffraction spectroscopy (XPS).

## 5.2 Methods and Materials

### 5.2.1 Synthesis Technique

A series of RP oxides $Sm_{1-x}La_xSr_{1-x}Ca_xNiO_{4-\delta}$ (x = 0.00, 005, 0.10, 0.15 and 0.20) were prepared through conventional solid state reaction process with initial reagents samarium oxide ($Sm_2O_3$: purity 99.9%),Lanthanum Oxide ($La_2O_3$: purity 99.9%),Strontium carbonate ($SrCO_3$: purity 99%), Calcium Carbonates ($CaCO_3$: purity 99.5%) and Nickel Oxide (NiO: purity99%) weighed in Stoichiometric amounts and properly mixed in agate mortar with acetone for 8-10 hours in order to produce uniform dense ceramics. The obtained powder was calcined in air at 1200 ˚C for 3h. The calcined powder was then mixed well in an agate mortar and mixed with 2% polyvinyl alcohol (PVA) as a binder. Further, the calcined powder was pelletized in hydraulic pellet press via cylindrical die-set under the uniaxial pressure of 4-5 $Kg/m^2$. The obtained pellets were sintered at 1250˚C temperature for 3h. The heating rate of the calcination and sintering process was maintained 5˚/min.

### 5.2.2 Characterization Techniques

TGA measurement (Mettler Toledo, Germany) was performed from Room temperature (RT) to 1273 K with heating rate of $5^0$/ min to study the weight loss. X-Ray powder diffraction pattern was performed through Rigaku Miniflex II desktop with Cu-Kα radiation (λ ~ 1.5406 Å) was used to determine the phase formation samples at RT in the range 20º-70º with a step of 0. 01º.The FTIR spectroscopy was implemented in ATR mode via Nicolet iS5. The spectral range of the FTIR analysis was 550 to 2000 $cm^{-1}$. The surface morphology was analyzed through scanning electron microscopy (EVO- Scanning Electron Microscope MA15/18) and the element constituent was analyzed through EDAX analysis. The electrochemical performance of all the sintered samples was investigated by cyclic voltammetry using three - electrode system in 1 M KOH alkaline medium. For three electrode system, Ag/AgCl electrode was choose as reference electrode whereas Pt wire as counter electrode and sample as a working electrode. All the desirable parameters such as specific capacitance, EDLC were extracted though CV data. Finally, the chemical and elemental compositions of the surface of these samples were analyzed through XPS by using the KRATOS, Amicus model under the pressure of $10^{-6}$pa using Mg target.

## 5.3 Results and Discussion

### 5.3.1 Thermogravimetry analysis

The thermal decomposition mechanism of all the compositions is examined by TGA analysis in an $O_2$ atmosphere, as shown in fig. 5.1. The gradual mass loss is observed with the temperature from TGA graphs of all the samples. Furthermore, the derivative of mass loss with temperature ($\frac{dm}{dT}$) vs T was studied for clarification regarding the decompositions of samples.

Two sharp humps are observed in the sample with x = 0.15 at 653K and 1048K, and for sample with x = 0.20 at 578K and 973K. These humps are corresponding to CO and $O_2$ loss, respectively. Despite of some irregular hump, a sharp hump is observed in the sample with x = 0.00 at 450K and for the sample with x = 0.05 at 473K. This hump is indicating the CO loss in both samples. Interestingly, a sharp kink is observed in sample with x = 0.10 at ~1028K. This is indicating the mass gain in sample which can be coupled with the change of oxygen stoichiometry (δ)[234]. This mass gain may be attributed to the re-oxidation process of Ni in x = 0.10. The positions of the kinks observed in $\frac{dm}{dT}$ curves are consistent with the mass loss curves.

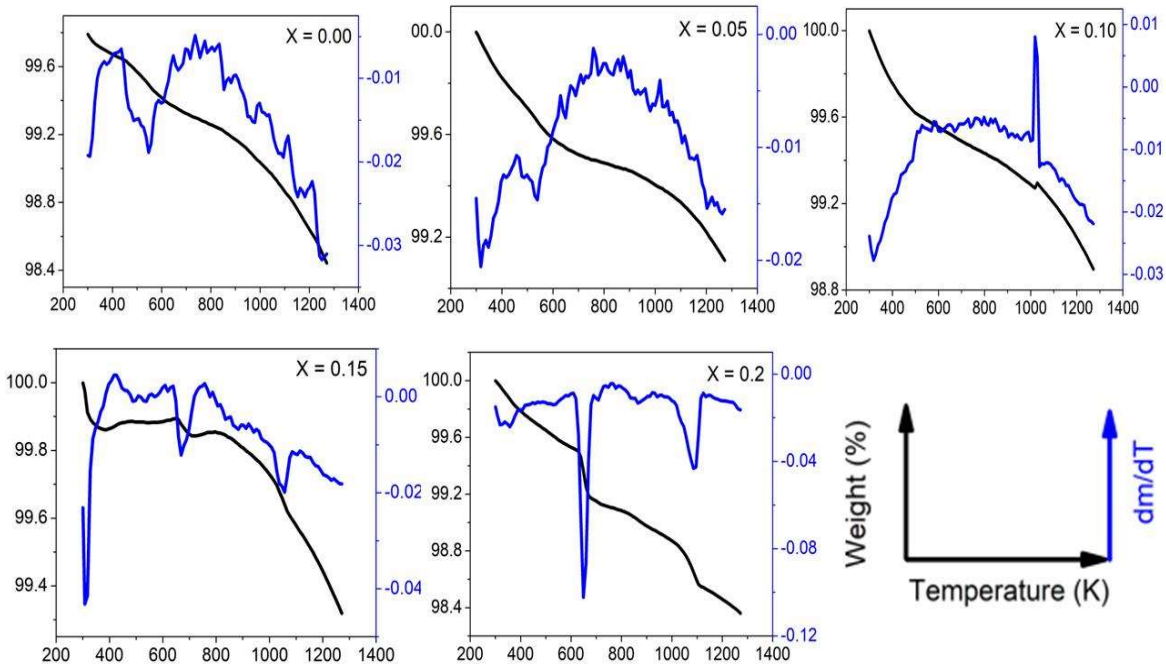


**Figure 5.1:** TGA and dm/dT variation of $Sm_{1-x}La_xSr_{1-x}Ca_xNiO_{4-\delta}$ (x = 0.00, 0.05, 0.10, 0.15, 0.20)

## 5.3.2 Structural and microstructural studies

### 5.3.2.1 XRD analysis

The X-ray diffraction graph of all the sintered samples is shown in fig. 5.2 (a). All the compositions have the similar peak as of the parent sample x = 0.0, as no additional peak was observed. As the doping of $La^{+3}$ on A-site and $Ca^{+2}$ on A'-site increased, the major peak shifted towards a higher angle from x = 0.05 to x = 0.15, and after that, the major peak shifted towards a lower angle for x = 0.20. This is due to the higher ionic radii of $La^{+3}$ (1.216Å) than $Sm^{+3}$ (1.132Å). In order to confirm the phase formation, Rietveld refinement was performed of X-ray diffractograms with Full Prof Suite package using peak profile Thompson–Cox–Hastings pseudo-Voigt function with axial divergence symmetry and instrumental correction. All the samples are well refined with tetragonal phase and I*4/mmm* symmetry. The goodness of fit factor i.e., $\chi^2$ and other refinement factors are confirming the well refinement (fig. 5.3(a)). With the variation of the compositions, the lattice parameters and volume decrease in all the samples as compared to sample with x = 0.00 (fig. 5.3). This is indicating that $La^{+3}$ and $Ca^{+2}$ successfully replaced $Sm^{+3}$ and $Sr^{+2}$ and entered in the lattice. This is also reflecting in the overall ionic radii of A-site as it also decreases with the substitution. After co-doping, the lattice shrinks for all of the samples. The non-uniform variation of the lattice parameters and the volume with compositions is because of the different ionic radii of A and A' site cations, which can play different roles.

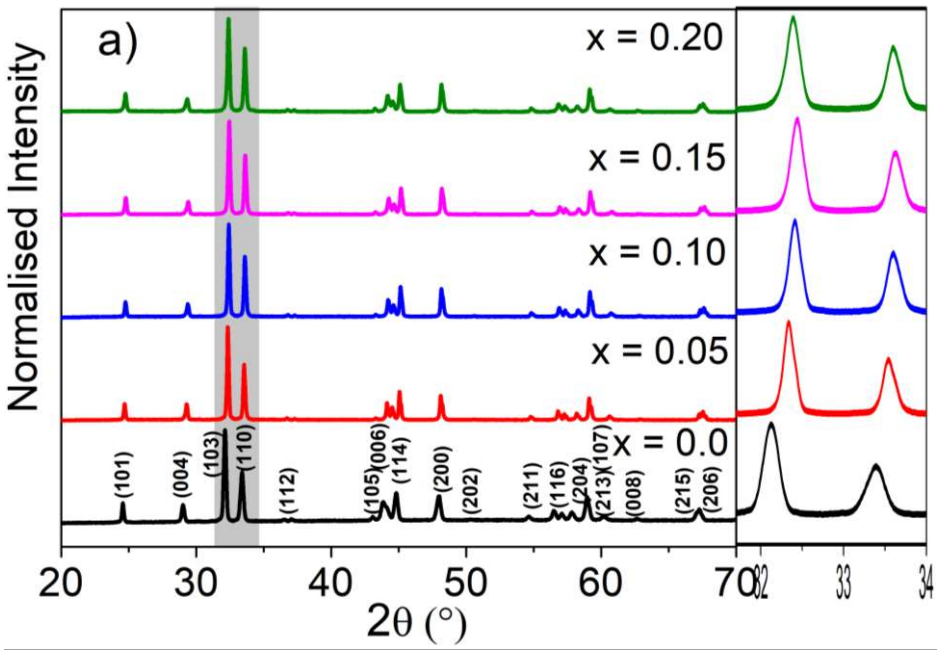


**Figure 5.2:** The X-ray diffractograms of the sintered $Sm_{1-x}La_xSr_{1-x}Ca_xNiO_{4-\delta}$ (x = 0.00, 0.05, 0.10, 0.15, 0.20)

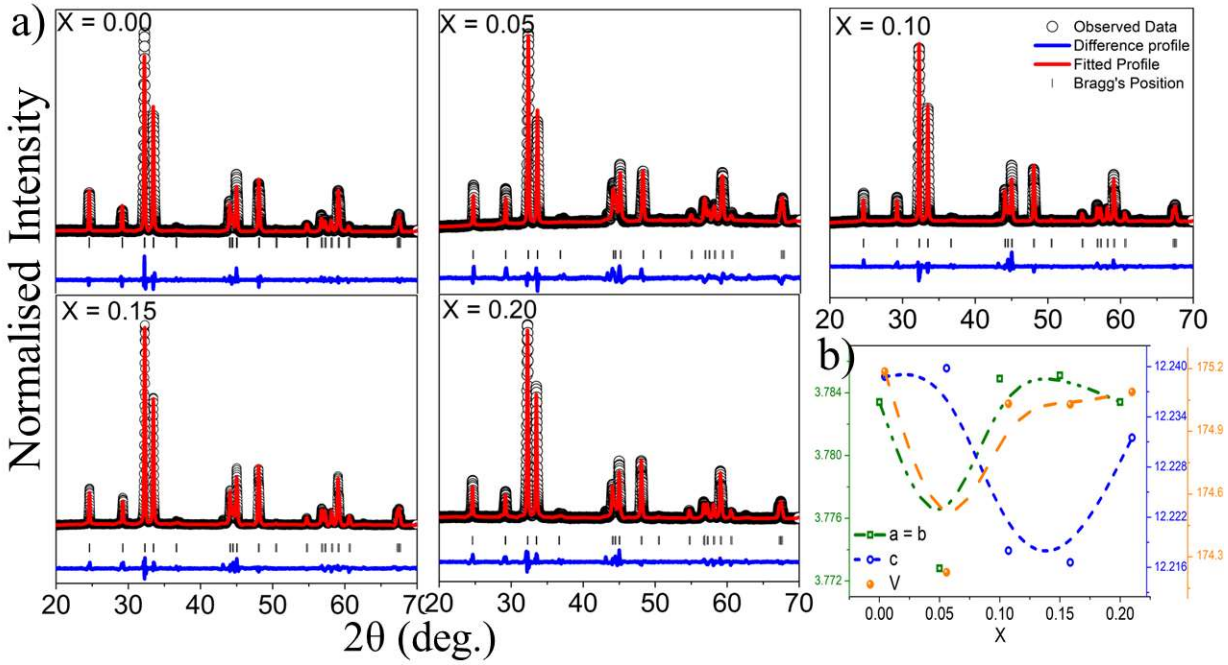


**Figure 5.3:** (a) Rietveld refinement of the sintered $Sm_{1-x}La_xSr_{1-x}Ca_xNiO_{4-\delta}$ (x = 0.00, 0.05, 0.10, 0.15, 0.20) and (b) Lattice Parameters and volume variation of $Sm_{1-x}La_xSr_{1-x}Ca_xNiO_{4-\delta}$ (x = 0.00, 0.05, 0.10, 0.15, 0.20)

### 5.3.2.2 FTIR analysis

FTIR transmission spectra were used to investigate the formation of oxide band groups and hydroxyl band groups. Fig. 5.4 shows the FTIR spectra of the all the samples with baseline correction over the spectral range of 550 to 4000 $cm^{-1}$. Only hydroxyl band groups are present above 2000 $cm^{-1}$ in the FTIR spectra of the composition with x = 0.00 sample, and a typical Ni-O signature is also visible in the fingerprint region (400-1400 $Cm^{-1}$), particularly the absorption band at ~550 $cm^{-1}$. For sample with x = 0.00, α-$Ni(OH)_2$ is observed while other samples (x = 0.05, 0.10, 0.15 and 0.20) of the series show the presence of γ-NiO(OH). The -OOH group is present at ~2000-2500 $cm^{-1}$ in samples with x = 0.05, 0.10, 0.15, 0.20 while for sample with x = 0.00, -OH group is present at ~2900 $cm^{-1}$ [229].

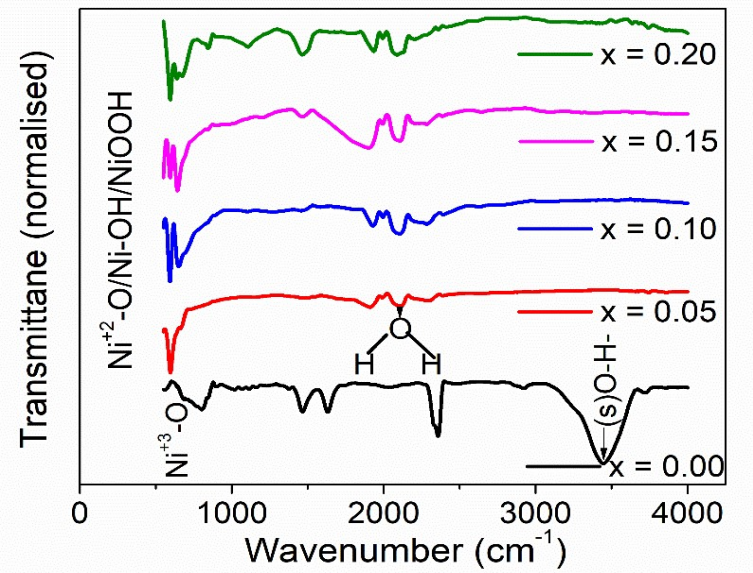


**Figure 5.4:** FTIR specta of the samples $Sm_{1-x}La_xSr_{1-x}Ca_xNiO_{4-\delta}$ (x = 0.00, 0.05, 0.10, 0.15, 0.20).

### 5.3.2.3 Microstructural studies

The microstructural analyses of all the samples were characterized by SEM and element component through EDX analysis, as shown in fig. 5.5. The grain size histograms are shown in the relevant insets. The presence of Sm, Sr, Ni, O, La, and Ca in the EDX data of all the samples confirms the stoichiometry composition of all the compounds. Porosity can be seen throughout the surface of all the samples. The grain size varies in indirect proportion to the concentration of Ni in each sample, which is an intriguing finding. In x = 0.10, the oxygen content is maximum, but the grain size is smallest. The nickel level is highest in sample x = 0.20, whereas the oxygen content is lowest. The porosity was determined using the relation Porosity (%) = $(1-\frac{Exp.density}{Th.density})\times 100$ (Fig. 5.7). The maximum porosity is for composition x = 0.10 (≈ 58.84 %), which is associated with the sample's smallest particle size. Porosity is an important attribute of cathode materials, as it considerably improves the charge-transfer process because of the good availability of electrolyte close to the surface and large effective surface area. The stoichiometric calculations of all the elemental content are well matched with the experimental EDAX, within an error of 5%. (Fig. 5.6) shows the comparison of stichometry and EDAX data of Oxygen content for all the compositions. All of the samples are deficient in oxygen, but x = 0.10 has the highest oxygen percentage, the similar pattern can be seen also in the TGA results (Fig.5.1).

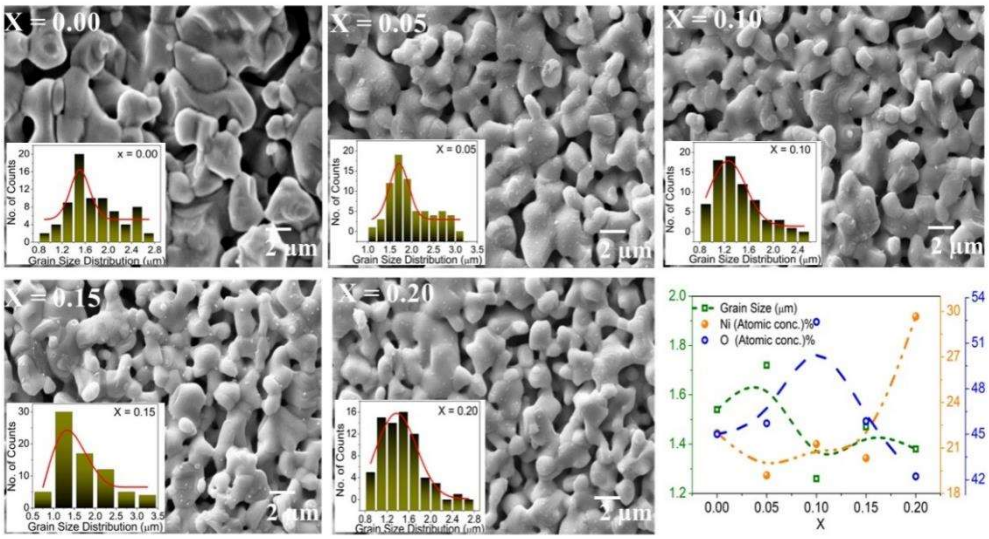


**Figure 5.5:** SEM Micrographs and the grain size histogram (inset) for $Sm_{1-x}La_xSr_{1-x}Ca_xNiO_{4-\delta}$(x = 0.00, 0.05, 0.10, 0.15, 0.20).

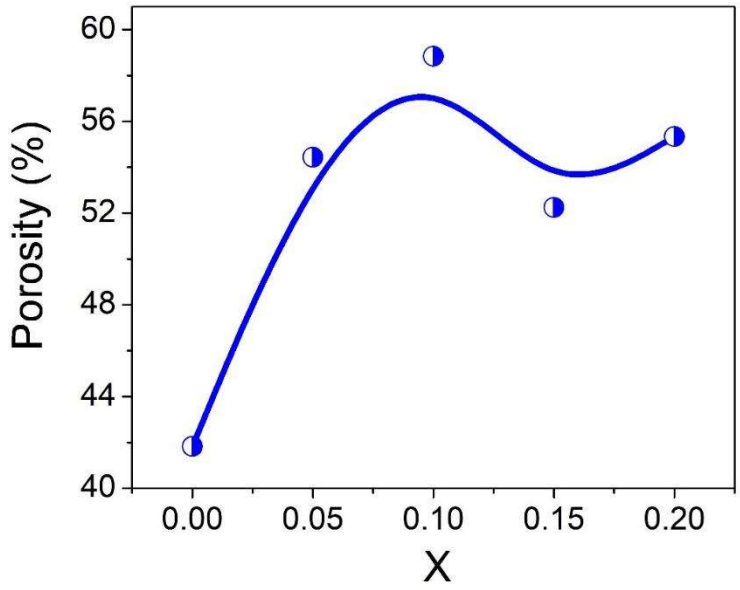


**Figure 5.6:** Porosity of $Sm_{1-x}La_xSr_{1-x}Ca_xNiO_{4-\delta}$ (x = 0.00, 0.05, 0.10, 0.15, 0.20)

## 5.3.3 Electrochemical properties

### 5.3.3.1 OER and ORR activity

Catalytic activities of all the synthesized samples for ORR and OER were investigated using cyclic voltammetry (CV) in potential range -1.5 V to +1.5 V. The CV data is recorded on forward scan (low potential to high potential) and backward scan (high scan to low scan). Forward scan is oxidative scan and gives information of anodic peak current and peak potential (observed in $I^{st}$ or $II^{nd}$ Quadrant) and generally associated with OER activity[122]. Similarly, backward scan is reductive scan, which informs about cathodic peak current and peak potential (observed in $III^{rd}$ or $IV^{th}$ Quadrant) and generally associated with ORR activity. Fig. 5.8(i) represent the CV curve of all the samples at scan rate of 30 mV/s in 1 M KOH alkaline solution. A slight of reduction peak ($III^{rd}$ Quadrant) is observed in the sample with x = 0.00 and x = 0.05 with no signature of oxidation peak. However, a strong reduction peak appears in CV curve of the sample with x = 0.10, 0.15 and 0.20. This can be described by the formation of nickel ion in electrolyte solutions and reversible faradic reaction between the $Ni^{2+}$and $Ni^{3+}$. On the other hand, a peak of oxidative current ($I^{st}$ Quadrant) is followed by the sharp rise in catalytic current in sample with x = 0.10 and 0.15, which can be accompanied by the generation of oxygen bubble in the surface of working electrode. In addition, the oxidation and reduction peaks are shifted towards the lower potential from x = 0.10 to x = 0.20, which is indicating the improved reaction kinetics [235]. The CV curve of sample with x = 0.10 and x = 0.20 is showing the pair of redox peaks. A pair of redox peaks observed in CV curve is attributed to the redox reactions and indicating the characteristics of pseudo-capacitance [236]. However, for a large region of potential range, there is no peak in CV curve which also indicates the presence of capacitive reaction in samples [237]. The capacitive behavior in these samples is originated because of

the conversion between the different oxidation states of nickel. This is indicating the combination of pseudo capacitance and electrochemical double layer capacitance (EDLC) in these two electrodes.

CV curve of the samples was also performed at various scan rates (Fig.5.9) but only two scan rates mainly 30 and 250 mV/sec are presented in fig. 5.8(ii). With the increase of scan rate, the peak current density increases in all sample. This is a common phenomenon which indicates the rapid rate of ionic and electronic transport. No specific change in the shape of CV curve with the variation of scan rate (Fig. 5.8(ii)), indicating the improved mass transportation with good electron conduction[238]. However, at high scan rate, samples with x = 0.10 and 0.20 show the asymmetric CV curve.

The difference between the cathodic and anodic peak ( $\Delta E_p$ ) is calculated for all the samples at a scan rate of 30 mV/s (fig.5.10). $\Delta E_p$ can be correlated with the reversibility of the electrode reactions. The low value of $\Delta E_p$ indicates the better reversibility features[239]. It can be seen in fig.5.10 that the composition with x = 0.10 has smallest value of $\Delta E_p$. This is also implying the fact that sample with x =0.10 should have high capacitance among all the samples.

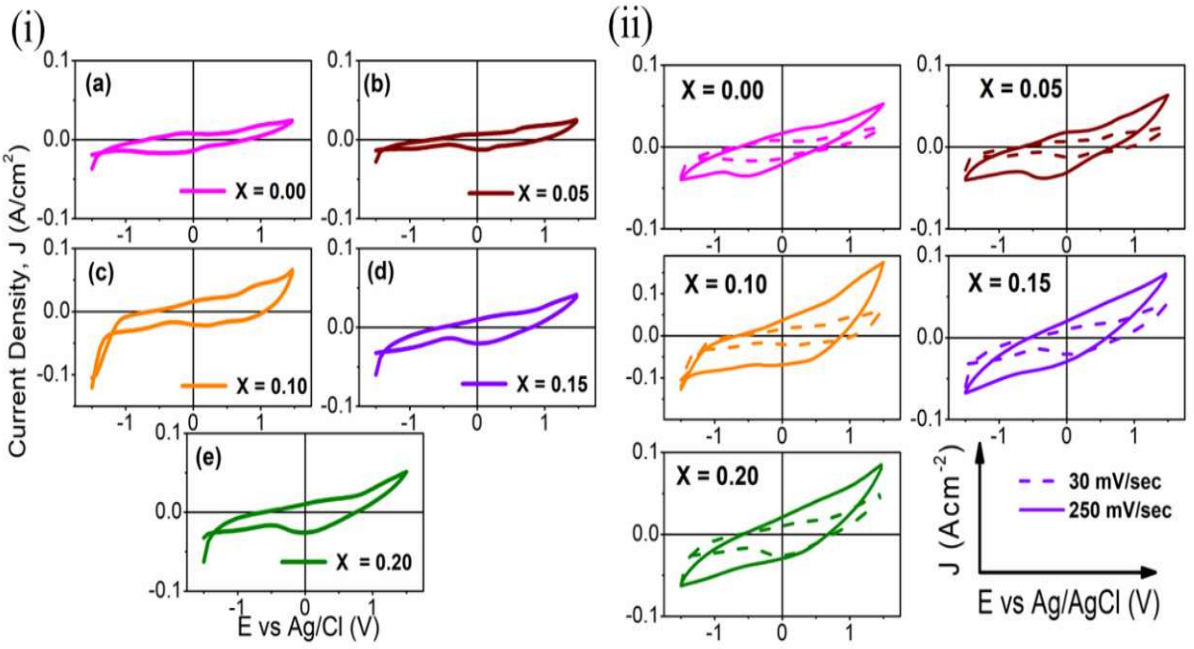


**Figure 5.7 (i)**: CV curve of all the sample at a scan rate of 30 mV/s **(ii):** CV curve of all the electrode samples at different scan rates

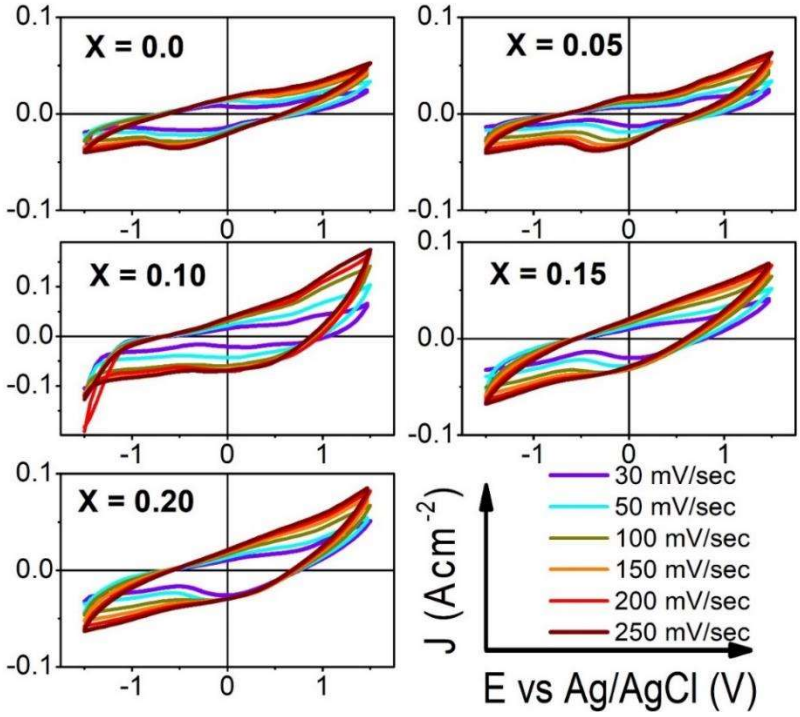


**Figure 5.8:** CV curves of $Sm_{1-x}La_xSr_{1-x}Ca_xNiO_{4-\delta}$ (x = 0.00, 0.05, 0.10, 0.15, 0.20) at different scan rates.

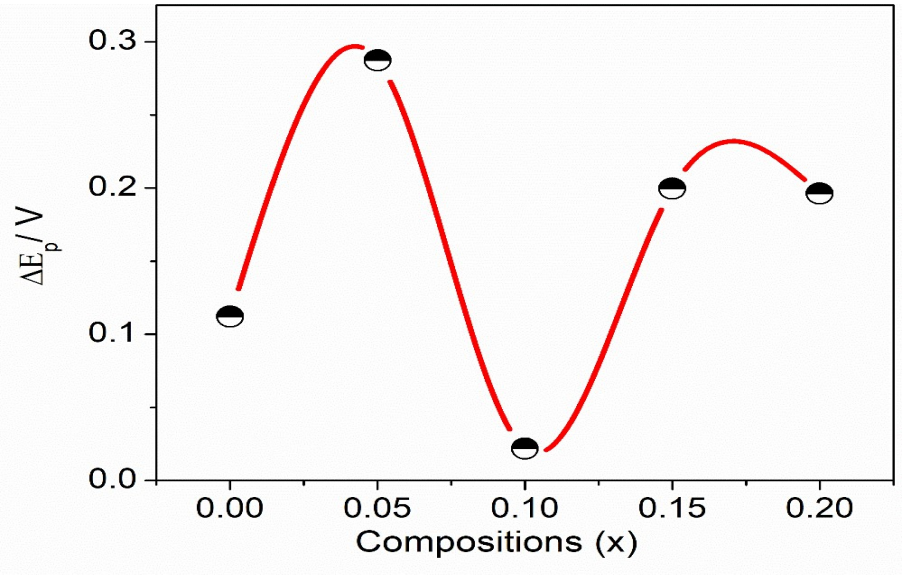


**Figure 5.9:** Variation of $\Delta E_P$ with compositions for all electrode samples.

### 5.3.3.2 Specific Capacitance

The specific capacitance has been calculated for all the electrode samples by using the relation:

$$C_p = \frac{\int I(v)dv}{mv\nabla V} \qquad (5.1)$$

Here, $\int I(v)dv$represents the area under the curve in CV graph, m represent the mass of the active electrode (in gm), $v$ indicates the scan rate and $\nabla V$ represent the potential window(-1.5 V to +1.5 V) [240]. The variation of specific capacitance with scan rate for all the electrode sample is shown in (fig.5.11). The value of specific capacitance decreases with scan rate following the de- Levie effect of electrode[241]. This pattern might be because of the presence of those inner active sites, which doesn't sustain the redox transition completely resulting the low electrochemical utilization of the electrode materials[242]. The better reversibility features of sample with x = 0.10 is also reflecting on its capacitive behavior. Sample with x = 0.10 has

highest specific capacitance (910.20 F/g) among all synthesized electrodes. The high value of specific capacitance is attributed to the maximum reversible redox process for charge storage as well as diffusion and ion penetration for faster electrode kinetics[242]. However, all other compositions also have a better capacitance value. A comparative of specific capacitance of synthesized electrodes with other reported electrodes is shown in table 5.1.

**Table 5.1:** Comparison of specific capacitance of several reported electrode with present work

| | Cell configurations | Electrolyte molarity (KOH) | Specific capacitance (F/g) | Reference |
|---|---|---|---|---|
| **$La_2NiO_{4-\delta}$** | Three-electrode | 3 M | 657.4 | [9] |
| **$LaSr_2Mn_2O_7$** | Three-electrode | 0.1 M | 167.2 | [11] |
| **$Sr_2SnO_4$** | Three-electrode | N/A | 210 | [26] |
| **$Pr_{0.80}Ba_{1.20}Co_2O_{6-\delta}$** | Three-electrode | 1 M | 408.37 | [27] |
| **$SmSrNiO_{4-\delta}$** | Three-electrode | 1 M | 424.8 | **In this work** |
| **$Sm_{0.95}La_{0.05}Sr_{0.95}Ca_{0.05}NiO_{4-\delta}$** | Three-electrode | 1 M | 399.9 | **In this work** |
| **$Sm_{0.90}La_{0.10}Sr_{0.90}Ca_{0.10}NiO_{4-\delta}$** | Three-electrode | 1 M | 910.2 | **In this work** |
| **$Sm_{0.85}La_{0.15}Sr_{0.85}Ca_{0.15}NiO_{4-\delta}$** | Three-electrode | 1 M | 594.3 | **In this work** |
| **$Sm_{0.80}La_{0.20}Sr_{0.80}Ca_{0.20}NiO_{4-\delta}$** | Three-electrode | 1 M | 646.5 | **In this work** |

**Table 5.1:** Comparison of specific capacitance of several reported electrode with present work

### 5.3.3.3 Pseudocapacitive behaviour

The total charge store in electrode can be because of the either faradic contribution from charge transfer process (pseudo capacitance) or non-faradic contribution from the double layer contribution (i.e., EDL effect). The charge storage effect can be characterized from the CV data by using the general power law relationship given in the equation[243]:

$$i = av^b \qquad (5.2)$$

Where *i* is the total current, *v* is the scan rate and *a* and *b* are the constants. The value of *b* is very critical to define the kinetic information about the electrochemical reactions. In general, there are two well define conditions for the value of *b*. If *b* is equal to 0.5, the process is diffusion-controlled faradic process and it occurs in the crystallite frame work of electrode materials. On the other hand, if *b* is equal to 1, it signifies the contribution from fast near-surface activities. These actives can be charging/discharging of EDLC or fast surface redox reactions[240], [241]. The above two are the extreme cases defined for the value of *b*. However, if the value of b lies between 0.5 to 1, there is a mixed control of the electrode process, and no general boundary is defined for these transitions. The value of b for all the electrodes was calculated and shown in fig.5.12. The value of *b* is 0.69 for the compositions with x = 0.10 indicating the presence of mixed control of faradic and non-faradic process. However, the value is near of the 0.50 indicative the diffusion-controlled ion or electron transfer processes and current is mostly comes from pseudo-capacitive process. Besides that, all the other electrodes have *b* value less than 0.50, for which is there is no define parameter.

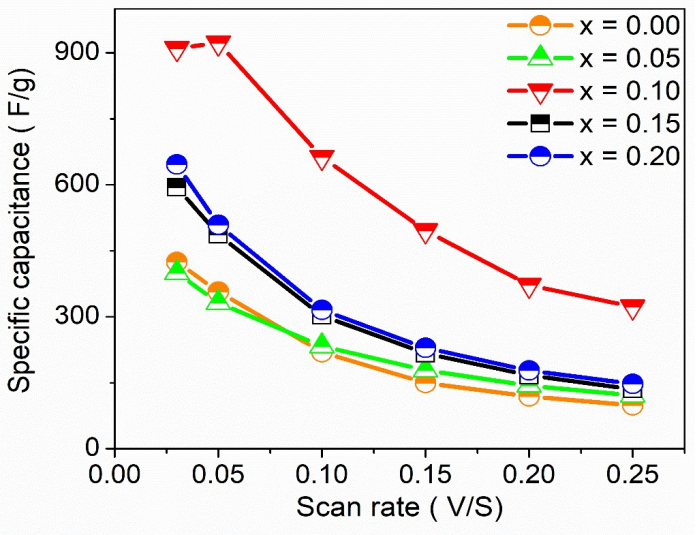


**Figure 5.10:** Variation of Specific capacitance with scan rate for all the electrode sample.

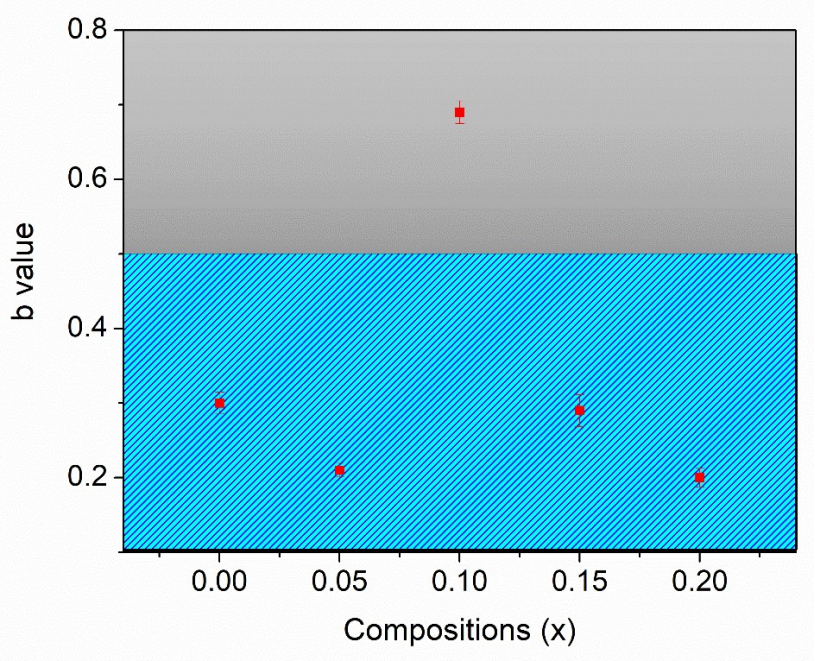


**Figure 5.11:** b-value plotted for all the compositions.

### 5.3.3.4 Electrochemical double layer capacitance

The electrochemical double layer capacitance ($C_{dl}$) is another parameter that can be extracted from the CV data. $C_{dl}$ of oxygen electrode catalysts is proportional to the active area of the catalyst. The sample with high value of $C_{dl}$ has high electrochemical active surface area (EASA) for catalytic activity. The value of $C_{dl}$ was calculated for all the electrodes in non-faradic region[244], [245] and shown in fig.5.13 (a). It is observed that $C_{dl}$ value for samples with x = 0.00, 0.05, 0.10, 0.15 and 0.20 is 55.94, 130.4, 238.25, 80.09, and 55.24 mF/cm$^2$ respectively. Among all the electrodes, sample with x = 0.10 has highest $C_{dl}$ value. This implies that electrode with x = 0.10 has best catalytic activity among all the electrode samples.

### 5.3.3.5 Electrochemical stability

In order to check the durability of all the electrode catalysts, chronoamperometry was performed under a constant voltage of +1 volt. The chronoamperometry behavior of all the samples is shown in fig.5.13 (b). It can be seen from the figure that despite slight fluctuation at starting, all the catalyst become stable for long time. The transient decay time was also calculated for all the sample and it was found that sample with compositions x = 0.10 has least decay time. This confirms the fact that compositions with x = 0.10 has best electrochemical activity among all the samples.

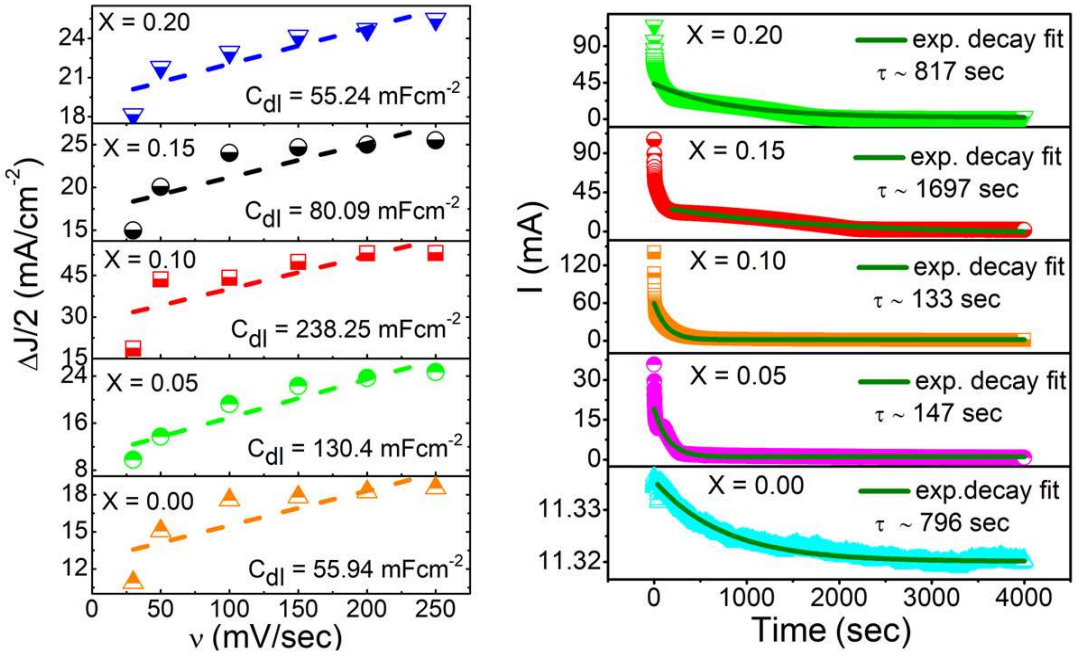


**Figure 5.12:** (a) value of $C_{dl}$ for all the electrode samples. (b) Chronoamperometry response of all the samples at 1 V

Since, the strong peak was observed only in the sample with x = 0.10 and x = 0.20 in CV graph (see fig. 5.8). The $\Delta E_P$ is also lowest in these two samples (see fig. 5.10). In addition, a remarkable electrochemical behavior (e.g., specific capacitance) is also observed in these two samples (fig. 5.11). Therefore, further analysis was performed on these two samples only. In

order to understand the mechanism of the better electrochemical behavior, electronic studies were performed in these two samples and on sample with x = 0.00 for reference.

## 5.3.4 Electronic Studies

### 5.3.4.1 XPS analysis

The electronic structure and chemical state of perovskite oxide catalysts have a significant impact on their electrochemical activity[246]. In order to investigate the good electrochemical behavior of samples, XPS measurement has been performed. XPS wide spectra and elemental spectra of individual elements were calibrated with carbon correction appearing at 285 eV. All the constituent elements and auger peaks of Ni and O are shown in wide spectrum and indexed according to the look up table (Fig. 5.15). In present system, Ni has variable oxidation state and oxygen non-stoichiometry playing an important role in electrochemical process. The deconvoluted peak of Sm3d, La3d, Sr3d, Ca2p, Ni2p and O1s with Shirley background of the samples with x = 0.00, 0.10, and 0.20 are shown in (Fig. 5.14).

Sm3d characteristics are in line with the standards. Furthermore, in the wide spectrum, $Sr3p_{1/2}$ overlaps with C1s. Sr3d state are split into two levels ($Sr_{5/2}$ and $Sr_{3/2}$) due to spin-orbit interaction with energy difference of 1.76 eV. Sr3d core level has two spin orbit split doublet. One is corresponding to the oxide (SrO) whereas second one is corresponding to the carbonate ($SrCO_3$)[229]. The XPS spectra of Ca 2p core level have also spin-orbit component with energy difference of 3.43 eV in sample with x = 0.10 [247]. Along with it, satellite features can also be seen in the Ca2p region. Two prominent satellite peaks present in Ca 2p spectra corresponding to $CaCO_3$[248]. Calcium is a highly reactive metal that is always present in the form of compounds such as calcium oxide or calcium hydroxide, which can react with $CO_2$ in the atmosphere to generate carbonates. The core peak of La3d is also split into two peaks $3d_{5/2}$

and $3d_{3/2}$. La is very reactive, it is typically found in an oxidized state, where it can combine with $CO_2$ to generate surface carbonates[249].

The deconvoluted XPS spectra of O1s for x = 0.0, 0.10 and 0.20 is divided into three characteristics peaks of oxygen species. The peak which is observed in the range of 528 to 530 eV (observed at 528.53 eV in our samples) is corresponding to the lattice oxygen ($O^{2-}$), whereas, the peaks which are located in the range of 530 to 532 eV (observed at 531.80 eV in our samples) are attributed to the dissociated oxygen on the oxygen vacancy [250]. Later, peak observed at 533.80 eV is corresponding to the auger peak [180]. For sample with x = 0.00, metal–O peak has higher intensity in comparison to that of with x = 0.10 and 0.20. Furthermore, the auger peak of O for sample with x = 0.00 is stronger than those of with x = 0.10, 0.20. This suggests that vacancy generation occurs more in composition with x = 0.00 than vacancy adsorbed in sample with x = 0.10, 0.20. This is in line with the TGA and SEM findings (Fig. 5.1 and Fig. 5.5). On the other hand, intensity of the oxidative oxygen species is higher in case of x = 0.10 as compared to the x = 0.00 and 0.20. This higher intensity indicates the increase of oxygen vacancy defect ($V_0$)[250]. Since high oxidative ion species ($O^{2-}/O^{-}$) formation is responsible for the improved OER activity as it provides the more active sites for catalyzing the OER[251], [252]. Therefore, it can be considered as one of the factors for good OER activity observed in sample x = 0.10 and also in good agreement with the CV and EASA results (Fig.5.8 and Fig.5.13).

Ni2p has a split spin-orbit component with a complicated structure as a mixture of metal, oxide, hydroxide, and satellite characteristics occur at ~ 17.3 eV. Multiplet splitting of Ni(metallic), NiO, and $Ni(OH)_2$ or Ni(OOH) is found for all three samples in this case, indicating that the Ni states are different. Ni2p has two deconvoluted peaks occurring around

~854 eV and 856 eV. These peaks are associated with $Ni^{2+}$(majorly from the NiO compound and detected on the surface of the materials) and $Ni^{3+}$ respectively[253]. It is observed that peak corresponding to $Ni^{3+}$ states has slightly shifted towards higher energy at x = 0.10 as compared to the x = 0.0 and x = 0.20. The intensity ratio of the $Ni^{3+}/Ni^{2+}$ is calculated for all the three samples and found that the ratio is highest in the case of the sample x = 0.10. This high ratio of $Ni^{3+}/Ni^{2+}$ in x = 0.10 indicates the enhanced Ni-O interaction. According to the previous studies, increased oxidation states of transition metal can enhance the electron transfer properties and also generate enhanced surface charge storage[254]. In addition, surface Ni with a higher oxidation state has a better covalent capability with lattice oxygen[255]. This is consistent with the better catalytic activity for the OER process in x = 0.10. Peak observed around ~858 eV in all three samples is corresponding to the hydro state of Ni (i.e. $Ni(OH)_2$ or Ni-OOH), but broadening of this peak is also giving a hint of the possible existence of $Ni^{4+}$state. However, peak feature of the $Ni^{4+}$cannot be easily resolved because of the close interaction. The peaks observed around ~861 eV and 864 eV are the satellite peaks of $Ni_{2p}$ and peak features are consistent with the previous studies[255].

Sm3d and Sr3d peaks do not shifts with binding energy although Ni-O and metal-hydroxide peaks do, indicating a change in oxidation states of $Ni^{2+}$ to $Ni^{2+\delta}$ and $O^{2-}$ to $O^{2-\delta}$ [229]. Therefore, it can be proposed that only Ni is participating in the oxygen intercalation process and faradic surface redox process for energy storage applications.

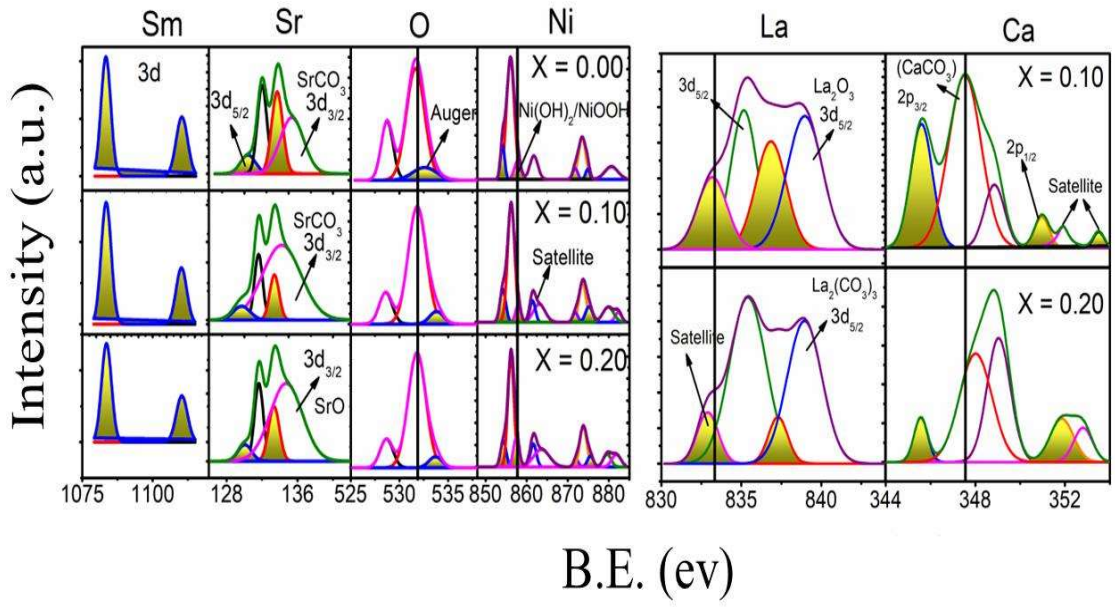


**Figure 5.13**: Deconvoluted XPS Specta using XPS peak 4.1 of Sm3d, Sr3d, La3d, Ca2p, Ni2p, and O1s with Shirley background of the samples $Sm_{1-x}La_xSr_{1-x}Ca_xNiO_{4-\delta}$ (x = 0.00, 0.10, and 0.20).

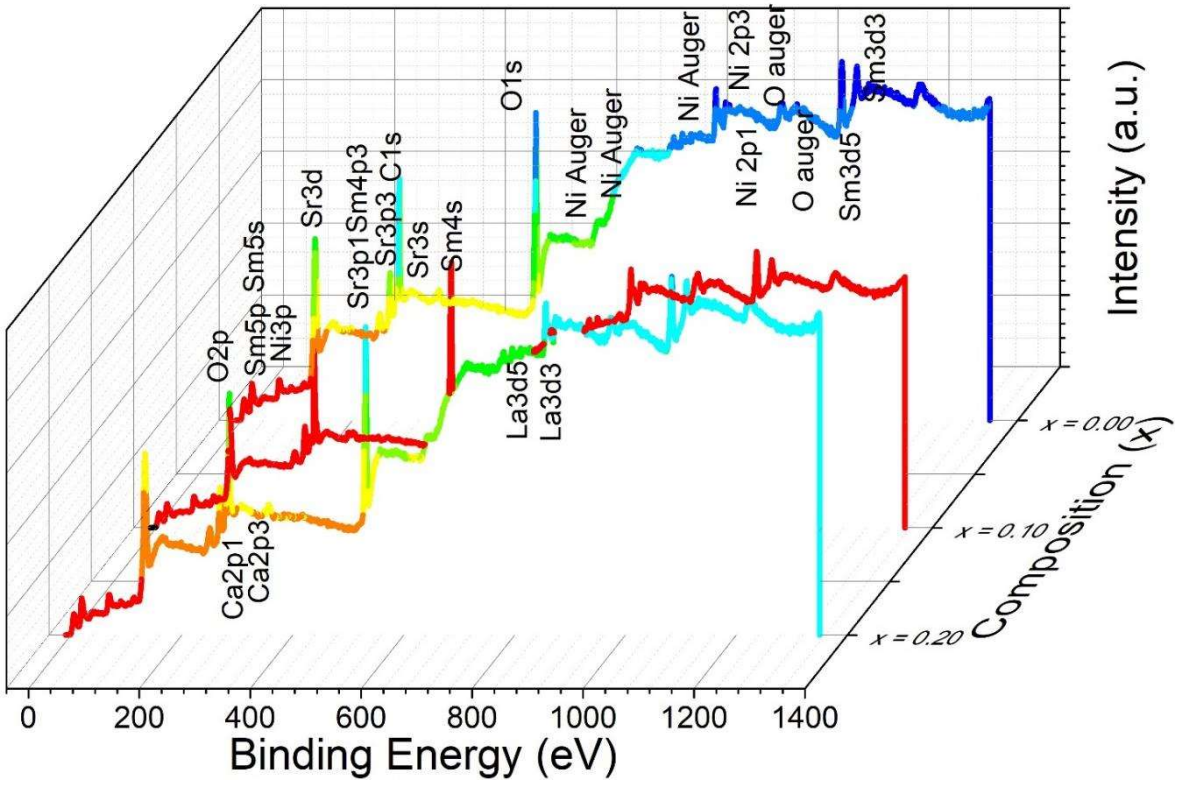


**Figure 5.14:** XPS wide spectrum of $Sm_{1-x}La_xSr_{1-x}Ca_xNiO_{4-\delta}$ (x = 0.00, 0.10, 0.20).

The mechanism of the intercalation, migration and redox process (for $Sm_{1-x}La_xSr_{1-x}Ca_xNiO_{4-\delta}$) can be described through the reactions (3) and (4), which comprises the three steps as follows:

(a) migration of oxygen interstitial ions along the edges of octahedral through the crystal[256]

(b) migration of oxygen ions between LnO layers[256]

(c) migration of apical oxygen ions from NiO octahedra to LnO layers creating apical oxygen vacancies and these vacancies are filled by those interstitial oxygen ions[257].

(i) Oxygen intercalation:

$$Sm_{1-x}La_xSr_{1-x}Ca_x\left[Ni^{2+}_{1-2\delta}/Ni^{3+}_{2\delta}\right]O_{4-\delta} + 2(\delta' + 1\,)OH^- \leftrightarrow$$

$$Sm_{1-x}La_xSr_{1-x}Ca_x\left[Ni^{2+}_{1-2(\delta+\delta')}/Ni^{3+}_{2(\delta+\delta')}\right]O_{4-\delta+\delta'} + (\delta' + 1)H_2O + 2(\delta' + 1)e^- \quad (5.3)$$

(ii) Faradic redox:

$$NiO + OH^- \leftrightarrow NiOOH + e^- \quad (5.4)$$

Where $\delta'$ is a dynamic oxygen over stoichiometric coefficient which, depends on the level of oxygen insertion. Oxygen intercalation leads the oxidation of $Ni^{+2}$ to $Ni^{+3}$, and yields water by the transfer of proton to electrolyte hydroxide ions[258]. This confirms that the redox processes in layered perovskites is associated with the valance change and oxygen intercalation.

## 5.3.5 Conclusion

A series of $Sm_{1-x}La_xSr_{1-x}Ca_xNiO_{4-\delta}$ (x = 0.00, 0.05, 0.10, 0.15, and 0.20) was successfully reported for the first time by using conventional solid-state route method and the effect of A-site substitution on $SmSrNiO_{4-\delta}$ was tested for electrochemical behavior in alkaline medium. All the samples are phase pure in tetragonal phase with I*4/mmm* symmetry as confirmed through XRD and Rietveld analysis. CV curve of all the samples at different scan rate reveals that samples with compositions with x = 0.10 ($Sm_{0.90}La_{0.10}Sr_{0.90}Ca_{0.10}NiO_{4-\delta}$) and with x = 0.20 ($Sm_{0.80}La_{0.20}Sr_{0.80}Ca_{0.20}NiO_{4-\delta}$) have a combination of pseudo capacitance and electrochemical double layer capacitance (EDLC). However, general power law reveals that all the sample excluded $Sm_{0.90}La_{0.10}Sr_{0.90}Ca_{0.10}NiO_{4-\delta}$ has the value of b parameter less than 0.50. only for the sample $Sm_{0.90}La_{0.10}Sr_{0.90}Ca_{0.10}NiO_{4-\delta}$, this value lies in the range of the pseudocapacitive materials. Further, a high value of specific capacitance (910.20 F/g) and electrochemical double layer capacitance (238.25 $mF/cm^2$) are observed in the same sample. XPS analysis revealed that oxygen and nickel play a crucial role on the high capacitive behavior of sample $Sm_{0.90}La_{0.10}Sr_{0.90}Ca_{0.10}NiO_{4-\delta}$. Formation of high oxidative ion species ($O^{2-}/O^{-}$) and high ratio of $Ni^{3+}/Ni^{2+}$in $Sm_{0.90}La_{0.10}Sr_{0.90}Ca_{0.10}NiO_{4-\delta}$ is resulting the enhanced electron transfer properties and also surface charge storage capacity. The study proves that $Sm_{0.90}La_{0.10}Sr_{0.90}Ca_{0.10}NiO_{4-\delta}$ is a suitable material for energy storage application to be used as a hybrid capacitor electrode.